Enhanced Mechanical, Thermal and Electrical Properties of High-Entropy HfMoNbTaTiVWZr Thin Film Metallic Glass and its Nitrides

Downloaded from: https://research.chalmers.se, 2022-10-11 19:43 UTC

Citation for the original published paper (version of record):
Alvi, S., Milczarek, M., Jarzabek, D. et al (2022). Enhanced Mechanical, Thermal and Electrical Properties of High-Entropy HfMoNbTaTiVWZr Thin Film
Metallic Glass and its Nitrides. Advanced Engineering Materials, In press.
http://dx.doi.org/10.1002/adem.202101626

N.B. When citing this work, cite the original published paper.

research.chalmers.se offers the possibility of retrieving research publications produced at Chalmers University of Technology.
It covers all kind of research output: articles, dissertations, conference papers, reports etc. since 2004.
research.chalmers.se is administrated and maintained by Chalmers Library

(article starts on next page)

ADVANCED ENGINEERING MATERIALS
www.aem-journal.com

Check for updates

Enhanced Mechanical, Thermal and Electrical Properties of High-Entropy HfMoNbTaTiVWZr Thin Film Metallic Glass and its Nitrides

*Sajid Alvi, Michal Milczarek, Dariusz M. Jarzabek, Daniel Hedman, Mojtaba Gilzad Kohan, Neonila Levintant-Zayonts, Alberto Vomiero, and Farid Akhtar**

The inception of high-entropy alloy promises to push the boundaries for new alloy design with unprecedented properties. This work reports entropy stabilisation of an octonary refractory, HfMoNbTaTiVWZr, high-entropy thin film metallic glass, and derived nitride films. The thin film metallic glass exhibited exceptional ductility of ≈60% strain without fracture and compression strength of 3 GPa in micro-compression, due to the presence of high density and strength of bonds. The thin film metallic glass shows thermal stability up to 750 °C and resistance to Ar-ion irradiation. Nitriding during film deposition of HfMoNbTaTiVWZr thin film of strong nitride forming refractory elements results in deposition of nano-crystalline nitride films with compressive strength, hardness, and thermal stability of up to 10 GPa, 18.7 GPa, and 950 °C, respectively. The high amount of lattice distortion in the nitride films leads to its insulating behaviour with electrical conductivity as low as 200 S cm^{-1} in the as-deposited film. The design and exceptional properties of the thin film metallic glass and derived nitride films may open up new avenues of development of bulk metallic glasses and the application of refractory-based high entropy thin films in structural and functional applications.

1. Introduction

Amorphous metallic alloys or bulk metallic glasses (BMGs) are non-crystalline metals that lack long-range order. The disordered atomic structure and absence of grain boundaries in BMGs results in giving them good soft-magnetic properties and excellent mechanical properties with high elastic limits and specific strength, as well as highly corrosion and wear-resistant properties.[1] Different BMGs based on Zr, Cu, Ti, Fe, Pd, Pt, and Au systems have been developed thus far.[1] However, one of the major drawbacks of BMGs is their low ductility. The concept of BMGs has been explored recently in developing thin film metallic glasses (TFMG) from vapor-to-solid phase deposition using binary or ternary compositions.[2,3] Furthermore, the composition window for achieving amorphous films is much wider than that achieved from BMGs using rapid casting as the resulting material from vapor-to-solid deposition is farther from equilibrium than the material produced by the liquid-to-solid casting process.[4] In addition to high strength, the resulting TFMG brings improved ductility and good formability.[4] Such thin films are useful in applications, such as biomedical use,[5] increasing fatigue properties of commercial blades,[6] microelectronics and optoelectronics,[7] wear resistance[8] and micro-electro-mechanical system (MEMS) devices.[9]

S. Alvi, D. Hedman, M. G. Kohan, A. Vomiero, F. Akhtar
Division of Materials Science
Department of Engineering Sciences and Mathematics
Luleå University of Technology
SE-971 87 Luleå, Sweden
E-mail: farid.akhtar@ltu.se

S. Alvi
Department of Physics
Chalmers University of Technology
SE-412 96 Göteborg, Sweden

M. Milczarek, D. M. Jarzabek, N. Levintant-Zayonts
Department of Mechanics of Materials (ZMM)
Institute of Fundamental Technological Research, Polish Academy of Sciences
02-106 Warsaw, Poland

D. Hedman
Research Center for Computational Design of Advanced Functional Materials
National Institute of Advanced Industrial Science and Technology (AIST)
Central 2, 1-1-1 Umezono, Tsukuba, Ibaraki 305-8568, Japan

D. Hedman
Center for Multidimensional Carbon Materials
Institute for Basic Science (IBS)
Ulsan 44919, Republic of Korea

A. Vomiero
Department of Molecular Sciences and Nanosystems
Ca' Foscari University of Venice
Via Torino 155, 30172 Mestre Venezia, Italy

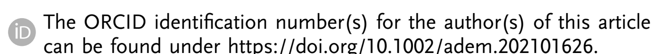
The ORCID identification number(s) for the author(s) of this article can be found under https://doi.org/10.1002/adem.202101626.

DOI: 10.1002/adem.202101626

 © 2022 Wiley-VCH GmbH

Amorphous metallic alloys based on four or more principal elements have been reported with a high thermally stable amorphous structure and superior mechanical properties.[10] The underlying mechanism of high thermal stability has been related to the high entropy of mixing and hindered phase transformation due to lattice distortion and sluggish diffusion. Liu et al. studied the effect of working argon (Ar) pressure and sputtering power on the glass formation ability of $Zr_{55}Cu_{30}Ni_5Al_{10}$ high-entropy TFMG, developed using sputtering of single targets in crystalline and amorphous forms.[11] The deposited films showed lower surface roughness with increased sputtering power and reduced Ar pressure. The composition and growth mode of the deposited high-entropy TFMG was found to be unaffected by the microstructure of alloy targets. Regarding the study of the mechanical properties of high-entropy TFMG, Zhao et al. studied the strain rate sensitivity of hardness in TiZrHfCuNi high-entropy TFMG.[12] The resulting film showed high strain rate sensitivity of hardness, increasing from ≈8.5 to ≈10.3 GPa, reflecting a homogenously disordered amorphous structure and high structure stability associated with the high-entropy effect. Similarly, Song et al. studied the effect of film thickness on the nanomechanical properties of TaNbHfZr medium high-entropy TFMG.[13] The resulting film showed an average hardness of 8 GPa, and indentation-induced phase transformation and pile-ups were found to be negligible in the thicker films, whereas plastic deformation in thinner films was severely affected by harder Si substrate. Fritze et al. studied the effect of substrate temperature from room temperature (RT) to 450 °C on the phase evolution and nano-mechanical properties of TiTaHfNbZr high-entropy films.[14] The resulting film showed phase evolution from an amorphous structure at RT to a single-phase BCC structure at 275 °C, followed by the formation of BCC + Laves phases at 450 °C. The resulting high-entropy TFMG showed an average hardness of 6.5 GPa and increased up to 9.2 GPa in crystalline high-entropy films. However, limited studies have been reported to investigate micro-compressional behavior and irradiation resistance of high-entropy TFMGs.

Similarly, extensive research on high-entropy nitride (HEN) films has also been carried out in developing nitride films with superior oxidation resistance and mechanical properties as compared to most of the reported conventional binary and ternary nitride films.[15] The use of multi-principle elements has enabled the freedom in choosing strong nitride-forming elements to develop nitride films with superior properties. The initial work of Yeh et al. showed that the super-hard (>40 GPa) and oxidation-resistant HEN films can be developed through the selection of strong nitride forming elements while applying appropriate substrate-bias and –temperature.[16–19]

The use of more than five principal elements can be beneficial for the formation of TFMG even at RT deposition due to high atomic-size differences. Furthermore, higher entropic stabilised TFMG can enhance the stability of the amorphous phase at a higher temperature. Previous works on high-entropy film with eight or more principal elements have shown the formation of an amorphous phase at 0% R_N (where $R_N = N_2/(N_2 + Ar)$), which changed to a face-centered cubic (FCC) solid solution with the increase in R_N.[20,21] Similarly, the hardness also increased with increasing R_N during deposition. However, the effect of using higher principal elements on nano-mechanical, high-temperature phase stability, electrical, and irradiation resistance properties has been rarely reported.

Based on these early works on high-entropy TFMG and its nitrides, we have developed octonary HfMoNbTaTiVWZr high-entropy TFMG based on strong nitride forming elements and derived nitride films using a partially sintered target. In this work, we have experimentally investigated the effect of high-entropy and lattice distortion on the thermal stability, nano-mechanical behavior, such as nano-indentation before and after Ar-ion irradiation, micro-compression properties, and electrical properties of high-entropy TFMG and its nitride films. The use of refractory elements with strong bonding between each other can enhance the mechanical- and electrical properties and irradiation resistance. The resulting high-entropy TFMG were found to have high thermal stability, -compressive strength, and -ductility. Furthermore, as all the chosen elements are strong nitride formers, high-entropy nitride films under different N_2 flow ratios were studied using in situ thermal stability and nano-mechanical properties. This study on octonary high-entropy TFMG and its nitrides has shown that utilization of high configurational entropy with strong bonding and nitride formation ability leads to thin films with superior thermal stability, mechanical- and electrical properties and enhanced irradiation resistance.

2. Results and Discussion

The X-Ray diffractograms of deposited HfMoNbTaTiVWZr high-entropy films with different R_N, together with density functional theory (DFT)-optimised special quasirandom structures SQS, is presented in **Figure 1**a. The deposited HfMoNbTaTiVWZr film at 0% R_N showed stabilisation of the amorphous phase and remained amorphous at 10% R_N. The amorphisation tendency at 10% R_N can be expected due to eight refractory elements, where the degree of atomic disorder and atomic size difference increases with an increasing number of elements.[22] The 30% R_N showed the formation of NaCl-type structure solid solution with a lattice constant of 4.37 Å, higher than that previously reported for high-entropy nitride films, as shown in Figure S1, Supporting Information,[17,23,24] and fits well with the simulated diffractogram of the DFT relaxed SQS of 4.38 Å. The increase in the number of elements can distort the lattice even further, resulting in an increased lattice constant. Furthermore, the incorporation of a higher mole fraction of N atoms results in fewer vacant sites on the FCC lattice, which in turn results in expansion of the unit cell and the lattice constant.[25] The grain size of 30% R_N film, calculated using Scherrer's equation, was found to be 17.5 nm. Cheng et al. has reported fine grain sizes in AlCrMoTaTiZr high-entropy nitride films, where insignificant grain growth is found to be related to the sluggish diffusion effect arising from the inefficiency of diffusion in multi-element films.[17]

The surface and cross-sectional SEM morphologies of HfMoNbTaTiVWZr high-entropy films deposited at different R_N as well as the EDS area analysis on the cross-section of films are presented in Figure S2 and Table S1, Supporting Information, respectively. The high-entropy films deposited at 0% R_N and 10% R_N showed featureless morphologies (Figure S2a,b, Supporting Information), which is typical of

© 2022 Wiley-VCH GmbH

ADVANCED ENGINEERING MATERIALS
www.aem-journal.com

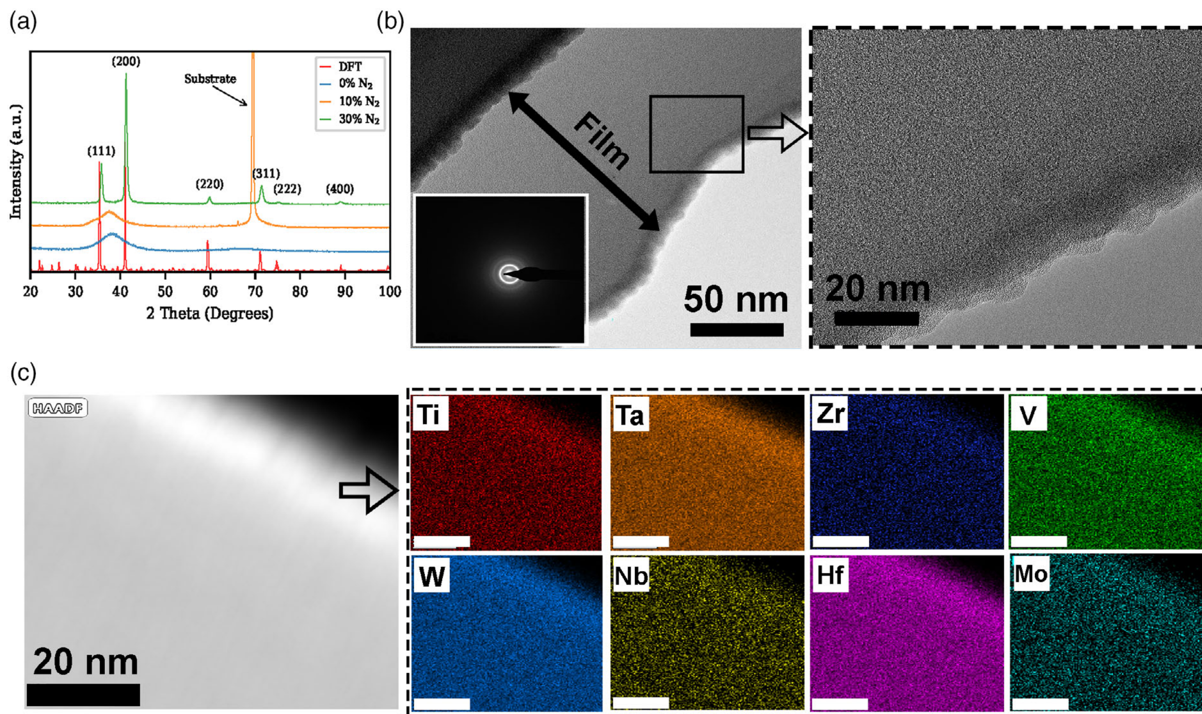

Figure 1. a) X-Ray diffractogram of HfMoNbTaTiVWZr high-entropy films at 0% R_N (blue line), 10% R_N (orange line), 30% R_N (DFT optimized: red line; experimental: green line); b) TEM micrograph of 0% R_N film cross-section with SAD pattern (inset) and its magnified micrograph, and c) HAADF elemental mapping across the cross-section of HfMoNbTaTiVWZr high-entropy TFMG (0% R_N).

amorphous films. The EDS area analysis of the film cross-section showed uniform distribution of elements (spots 1 and 2 of Table S1, Supporting Information). The morphology changed to a dense crystalline state with the formation of nano-grains at 30% R_N (Figure S2c, Supporting Information). It has been reported that insufficient energy of ions during deposition can lower the surface mobility of adatoms, leading to shadow effects and higher surface roughness.[16] In contrast, dense morphology arises from higher diffusivity of the atomic species on the surface, enhancing the filling of pores and voids. Such dense films are usually obtained with higher substrate temperatures or –bias during sputtering.[26] However, in 30% R_N high-entropy nitride film, the low sputtering yield of the target at higher nitrogen partial pressure and increase in interstitial nitrogen reduces the grain growth, resulting in dense film. Similar to the EDS area analysis of high-entropy nitride film at 10% R_N, 30% R_N film shows a uniform distribution of all of the elements with higher N content due to higher R_N (spot 3 of Table S1, Supporting Information). Figure 1b,c present the TEM micrographs with selected area diffraction (SAD) and high-angle annular dark-field (HAADF) elemental mapping of 0% R_N high-entropy TFMG. The TEM micrograph and SAD patterns show the formation of amorphous TFMG (Figure 1b). Furthermore, HAADF elemental mapping on the cross-section of the film shows uniform distribution of all refractory elements (Figure 1c).

The in situ high-temperature X-Ray diffractograms, along with the SEM micrographs of the films after high-temperature XRD analysis, are presented in **Figure 2**a. The HfMoNbTaTiVWZr high-entropy TFMG with 0% R_N shows the amorphous phase to be stable up to 750 °C, after which it partly crystallised at 800 °C. The high thermal stability of high-entropy TFMG can be related to the high configurational entropy, sluggish diffusion, and lattice distortion from eight refractory principal elements. Similarly, 10% R_N yields an amorphous structure in high-entropy nitride film, stable up to 750 °C, which then transforms to FCC solid solution at 850 °C and remains stable up to 1000 °C, along with the formation of minor oxide peaks of Ti and Zr (Figure 2a). The high-entropy nitride film with 30% R_N shows a NaCl-type solid solution structure, which is stable up to 950 °C, followed by delamination of the film at 1000 °C (Figure 2a). The delamination at 1000 °C relates to the coefficient of the thermal expansion and lattice mismatch between the high-entropy nitride film and Si substrate, resulting in delamination of the film rather than the oxidation of the film. The lattice constant in the 30% R_N film decreases from 4.41 to 4.38 Å with increasing temperature (Figure 2a). Such a decrease in lattice constant with increasing temperature has been previously reported on the thermal stability of high-entropy nitride film.[27] Huang et al. has reported the decrease in lattice constant in AlCrNbSiTiV high-entropy nitride film with increasing annealing temperatures up to 1000 °C due to the removal of point defects arising during sputtering deposition.[27] Furthermore, grain coarsening was not considered as the grain size increased from 19.1 to 21.4 nm with increasing temperature from RT to 700 °C, followed by decreasing to 16.4 nm at 950 °C. The decrease in grain size can be related to the removal of point defects and hindrance of grain growth due to lattice distortion.[27] However, the lattice strain increased after 700 °C, suggesting high residual stresses are generated in

 © 2022 Wiley-VCH GmbH

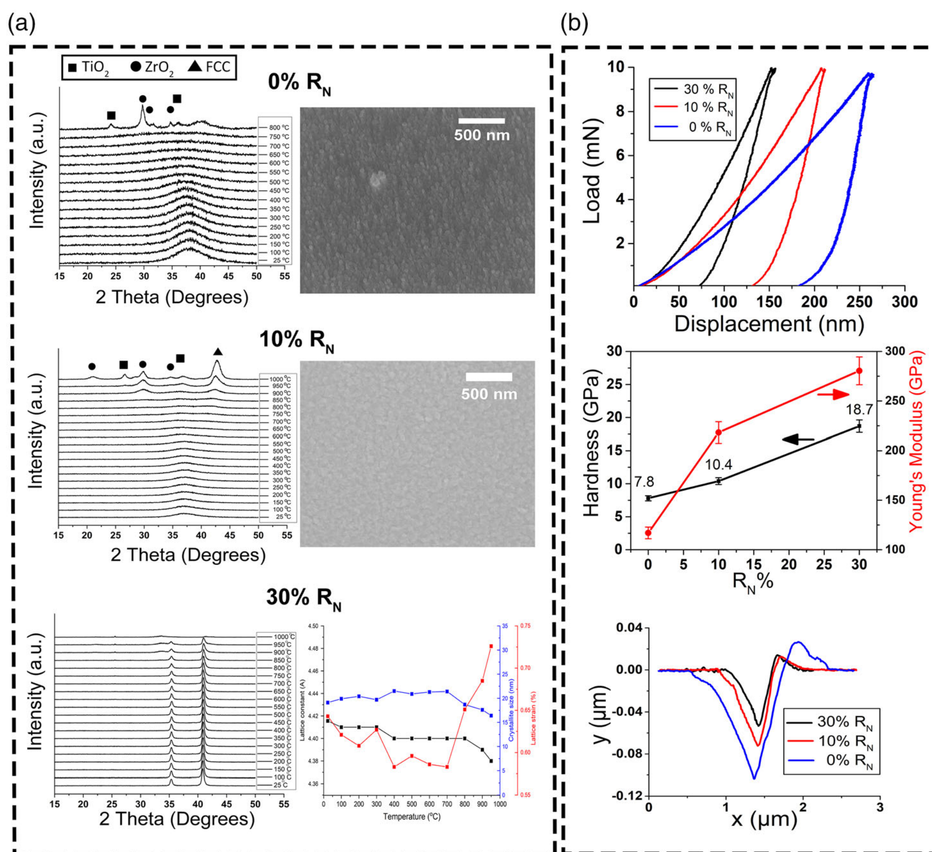

Figure 2. a) In situ high temperature X-Ray diffractograms and its corresponding SEM micrograph after the test of high-entropy films with 0% R_N, 10% R_N and 30% R_N, with plot showing the change in lattice constant, grain size and lattice strain with increasing temperature for 30% R_N; b) nanoindentation plots at 10 mN load, hardness and Young's modulus as a function of R_N, and its corresponding AFM indentation depth profiles.

the film.[17] The high residual stresses in the films resulted in the onset of delamination at 800 °C and were completely removed at 1000 °C. It can be noted that the patches of films still present on the substrate showed the presence of uniformly distributed elements from EDS point analysis on the SEM micrograph, as shown in Figure S3 and Table S2, Supporting Information.

The load versus depth profile plot shows a typical plot of increasing hardness values with increasing R_N (Figure 2b). The hardness of the films increases from 7.8 ± 0.3 GPa (0% R_N) to 10.4 ± 0.6 GPa (10% R_N), and finally to 18.7 ± 2.5 GPa (30% R_N). The lower hardness at 10% R_N, as compared to high-entropy nitride films reported in the literature, can be related to the lower mole fraction of N atoms for all the octonary refractory elements to form nitrides, which resulted in an amorphous structure. However, increasing the R_N to 30%, the N atoms form refractory nitrides and yield a NaCl-type solid solution structure, which in return provides high hardness.[28] Similarly, Young's modulus values increased from 117 ± 5 to 280 ± 10 GPa with increasing R_N, which is slightly lower than the DFT calculated value of 317 GPa for 30% R_N film. The Young's modulus of 30% R_N was found to be higher than previously reported HEN films deposited at RT and without substrate bias.[16,29] The comparison of AFM depth profiles after nanoindentation with different R_N showed the highest depth in 0% R_N, and the lowest depth in 30% R_N (Figure 2b). The utilisation of strong nitride forming refractory elements combined with lattice distortion and high-entropy effects imparts high hardness and Young's modulus values.

The engineering stress versus engineering strain plots of the micro-compression of pillars from each film with different R_N before and after annealing, and their corresponding SEM micrographs, are shown in **Figure 3**. The micro-compression of 0% R_N TFMG shows an average compressive strength and Young's modulus of 2.7 ± 0.1 and 59.9 ± 2.3 GPa, respectively. The morphology of the deformed pillars shows the formation of shear bands at the top part of the pillar, which is a classical deformation behavior of metallic glasses. BMGs have serrated plastic deformation due to the catastrophic growth of unhindered shear bands.[30] The load drops during plastic deformation in stress-strain curves of BMGs are usually observed due to nucleation and propagation of shear bands during the compression of pillars.[31] In contrast, the formation of shear bands in TFMG is limited, as the film thickness hinders the shear transition zones' (STZs) aggregation, and consequently provides much higher strength (>1–2 GPa) and improved compressive or tensile plasticity.[32] The engineering stress and engineering strain in 0% R_N TFMG after the yield point increased up to 4 GPa and 20%, respectively, where the compression was stopped before reaching

© 2022 Wiley-VCH GmbH

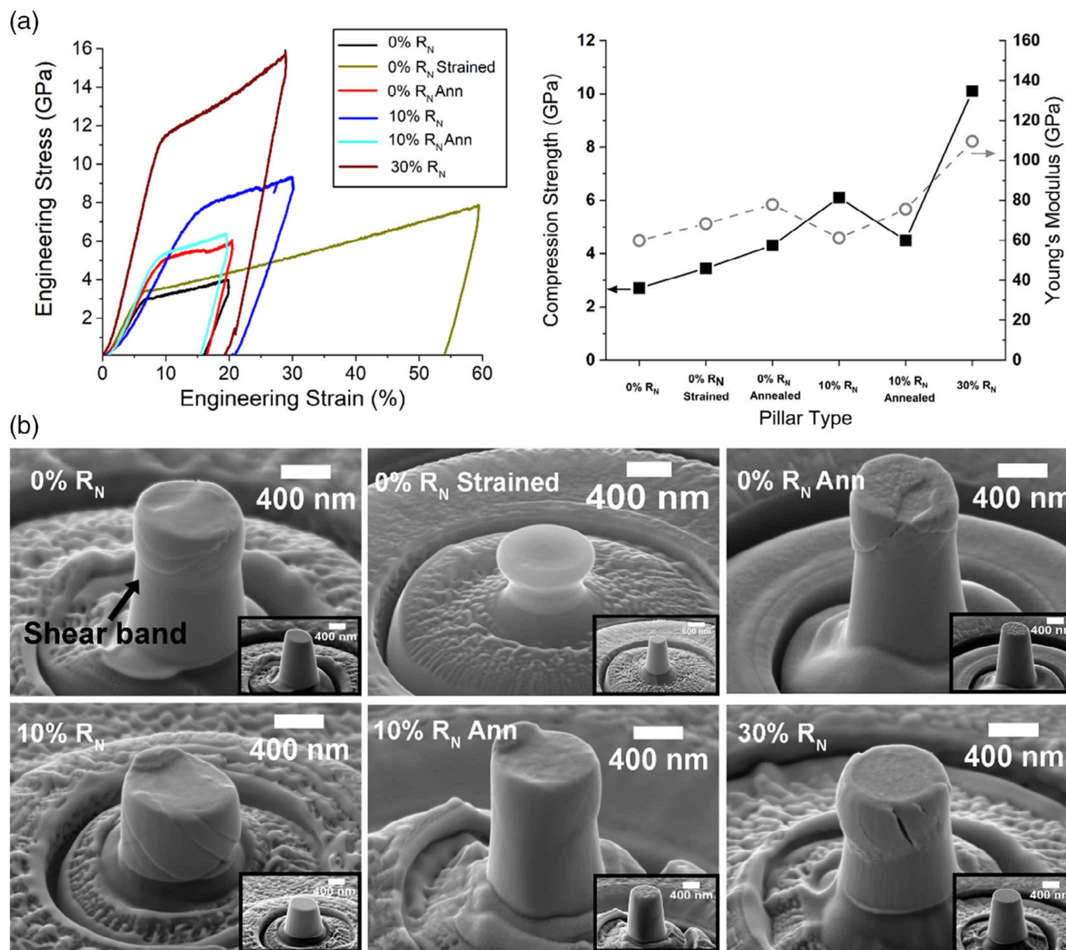

Figure 3. a) Engineering stress versus engineering strain plot with comparison of compression strength and Young's modulus from micro-compression of HfMoNbTaTiVWZr high-entropy films deposited at different R_N and annealing from in situ high temperature XRD analysis, and b) pillars before (inset) and after compression of HfMoNbTaTiVWZr high-entropy film with 0% R_N, 0% R_N strained to ≈60%, 0% R_N after in situ HT XRD at 800 °C, 10% R_N, 10% R_N after in situ HT XRD at 1000 °C and 30% R_N. (Ann: Annealed).

to the fracture of the pillar. Another pillar was compressed up to ≈60% strain to find the plasticity limit until fracture point (Figure 2b), and showed a compressive strength and maximum stress of 3.2 and 7.5 GPa, respectively. However, even in this case, the pillar did not go through fracture and rather acted like a gum-like material, as shown in the in situ recorded video during compression in Supplementary Video SV1, Supporting Information. The high amount of plasticity in 0% R_N TFMG and elasticity even after 60% strain suggests the presence of a strong- and high density-bonding. These results confirm that high-entropy-based TFMG far exceeds the strength and plasticity offered by binary- or ternary-based TFMG. Furthermore, to confirm that there was no stress-induced amorphous-to-crystalline phase transition in 0% R_N TFMG, EBSD was performed on the cross-section of the compressed pillars (Figure S4, Supporting Information), which did not show any kikuchi lines, suggesting the amorphous phase was retained even after micro-compression. The yield strength and Young's modulus of 0% R_N TFMG after annealing increased to 4.3 ± 0.1 and 77.9 GPa, respectively (Figure 3a). The two-fold increase in the yield strength can be expected due to the formation of mixed amorphous- and crystalline-phases. Furthermore, the compressed annealed pillars showed deformation in two primary shear bands, proving further that the annealed film has a higher concentration of amorphous phase.

The micro-compression of pillars from 10% R_N high-entropy nitride film shows an average yield strength and Young's modulus of 6.1 ± 0.6 and 61.0 ± 3.7 GPa, respectively, in Figure 3a. The resulting compressed pillars display typical amorphous deformation behaviour, with the formation of shear bands (Figure 3b). The engineering stress-strain plot from micro-compression in 10% R_N high-entropy nitride film after annealing up to 1000 °C shows an average yield strength and Young's modulus of 4.5 ± 0.5 and 75.5 ± 7.6 GPa, respectively (Figure 3a). The strength and modulus of the annealed film decrease due to the conversion from an amorphous- to crystalline phase along with the formation of minor oxides. The formation of a crystalline phase can change the deformation mechanism from shear band-based to dislocation-based deformation behaviour. Furthermore, the compressed pillar morphology showed the

© 2022 Wiley-VCH GmbH

formation of slip lines on one side of the pillar (Figure 3b). The use of micro-compression for understanding the stress-strain behaviour of hard coatings is a debated topic, due to resulting pillars with coarse surfaces arising from FIB milling, which may act as stress concentration points and alter the actual mechanical properties of pillars.[33] To minimize this, in 30% R_N high-entropy nitride film, a pillar surface with lower surface roughness was obtained after fine FIB milling (Figure 3b). The micro-compression in 30% R_N high-entropy nitride film shows an average yield strength and Young's modulus of 10.2 ± 0.4 and 110 ± 2 GPa, respectively, which are twice that reported for W, TiN, and VN films.[33] The resulting compressed pillar morphology shows preferential deformation in a vertical direction with a crack opening at the top part of the tapered pillar (Figure 3b). The compressed pillar shows considerable sustained plastic deformation after yielding, followed by an increase in stress up to 16 GPa until the onset of fracture. This high increase in stress after yielding and considerable plastic deformation of ≈30% strain is related to the work-hardening effect. Furthermore, the plasticity of compressed pillars with 30% R_N is even higher than the superhard Ti(C,N) and Zr(C,N) reported in the literature.[34] The high strength and modulus value can be expected in hard FCC solid solutions arising from octonary strong nitride formers, which can activate multiple slip systems to enhance strength and ductility.[35]

The deformation behaviour of nanocrystalline materials cannot be applied to TFMG due to the absence of grain boundary sliding and hindrance of dislocation movements. Rather, the strength and density of bonding govern the mechanical properties and thermal stability of TFMG.[36] The strength and ductility of high-entropy-based TFMG can be enhanced with a selection of elements giving rise to high configuration entropy, and high density of strength and bonding between each other, such as the octonary refractory elements chosen in the current work. Using this concept, HfMoNbTaTiVWZr high-entropy TFMG (0% R_N) displayed high hardness and compressive strength and extremely high ductility compared to other TFMG reported thus far. It has been reported that the increase in configuration entropy in metallic films and nitride film can enhance mechanical and thermal stability properties, especially in nitride film with the selection of strong nitride-forming elements.[35] Indeed, Jhi et al. have suggested that the nature of hardness in transition-metal carbides and/or nitrides can be determined more by the nature of bonding as compared to the observation of microstructural features that determine hardness in metals and alloys.[37]

The effect of Ar-ion irradiation on HfMoNbTaTiVWZr high-entropy films with different R_N flow ratios (0%, 10%, and 30%) was measured using multi-cycle nanoindentation analysis (**Figure 4**a). The Ar-ion irradiation on 0% R_N TFMG shows a slight increase in hardness of 1 GPa up to ≈80 nm indentation depth, after which the hardness remained unchanged. The low change in hardness values in 0% R_N TFMG can be explained by the fact that Ar-ion irradiation on crystalline metallic alloys and films tends to convert the surface region into an amorphous phase.[38] However, as-deposited 0% R_N TFMG having a fully amorphous phase can be less affected by Ar-ion irradiation. Furthermore, the slight increase in hardness can be related to the relaxation of the amorphous structure and the formation of small amounts of nanocrystals.[39,40] M. Iqbal et al. have reported the effect of Ar-ion irradiation with a similar ion dose as the current work on $Zr_{55}Cu_{30}Al_{10}Ni_5$ BMG, where the hardness increased by 30% due to the formation of crystalline phases.[41] In another work, H. Jia et al. have reported a similar phenomenon on the effect of Ar-ion irradiation on $Zr_{46}Cu_{37.636}Al_{8.364}Ag_8$ BMGs, however, they found 71% increase in hardness with an even lower Ar-ion dose of 8×10^{15} cm^{-2}.[39] In contrast, the hardness in 10% R_N nitride film decreased by ≈1.5 GPa up to 40 nm depth, followed by a decrease in ≈0.5 GPa up to 80 nm depth, after which hardness was found to be unaffected. The decrease in the hardness of 10% R_N nitride film after Ar-ion irradiation can be related to the conversion of nano-crystalline phases into amorphous phase, which can be deduced from the same hardness values of 0% R_N TFMG and 10% R_N nitride film after Ar-ion irradiation (≈10.3 GPa). Furthermore, the formation of new vacancies and void formation in amorphous nitride film can result in lowering the hardness values.[42] Whereas in 30% R_N nitride film, the hardness after Ar-ion irradiation increased by ≈3–11 GPa up to ≈80 nm indentation depth followed by similar hardness values to as-deposited film. The increase in hardness can be related to the formation of a new dense dislocation network below the irradiated zone and a reduction in grain sizes can further enhance the hardness of the 30% R_N nitride film.[43–46] It should be noted that the increase in nitrogen in films significantly decreases the disorder caused by ion irradiation. According to the SRIM simulations, a maximum displacement per atom (dpa) is equal to 292 for 0% R_N whereas for 30% R_N it is 175. On the other hand, the ion range is equal to 238 and 366 Å for 0% R_N and 30% R_N, respectively.

The variation in the electrical conductivity and resistivity of as-deposited HfMoNbTaTiVWZr high-entropy films with different R_N flow ratios (0%, 10%, and 30%) at different temperatures is shown in Figure 4b and S8, Supporting Information, respectively. The red curve represents the forward temperature ramp showing the change in electrical conductivity with increasing temperature from room temperature (RT, 23 °C) to 500 °C. Initially, the 0% R_N TFMG presented conductivity values of 7500 S cm^{-1} at RT, comparable to BMGs and higher than metallic high-entropy films.[47–49] The slight increase in the conductivity values (average conductivity of 7612 S cm^{-1}) of the films at temperatures of 100–250 °C can be assigned to stress relaxation in the film.[50] Subsequently, the electrical conductivity of the sample drastically drops by ≈46% with the increase in temperatures from 345 to 500 °C possibly due to the amorphous to the crystalline transition of the film. Increasing the R_N flow ratio to 10% and 30% in the films resulted in lower electrical conductivity values, where 30% R_N nitride film showed a 30 fold lower conductivity compared to 0% R_N TFMG. Interestingly, the addition of nitrogen to the high-entropy film resulted in a prompted shift of the crystalline transition temperature in the coatings. Consequently, the transition in the 0% R_N TFMG takes place at 345 to 500 °C range, whereas in the 10% R_N nitride films the transition is observed after 470 °C regions. High-entropy HfMoNbTaTiVWZr TFMG having moderate high electrical conductivity was found to be higher than the reported high-entropy films,[51] and the nitride films with very low electrical conductivity, in the range of 200–1100 S cm^{-1} after heating to 500 °C, comparable to insulating materials make them applicable in micro-electronics applications.[52] The extremely low electrical

© 2022 Wiley-VCH GmbH

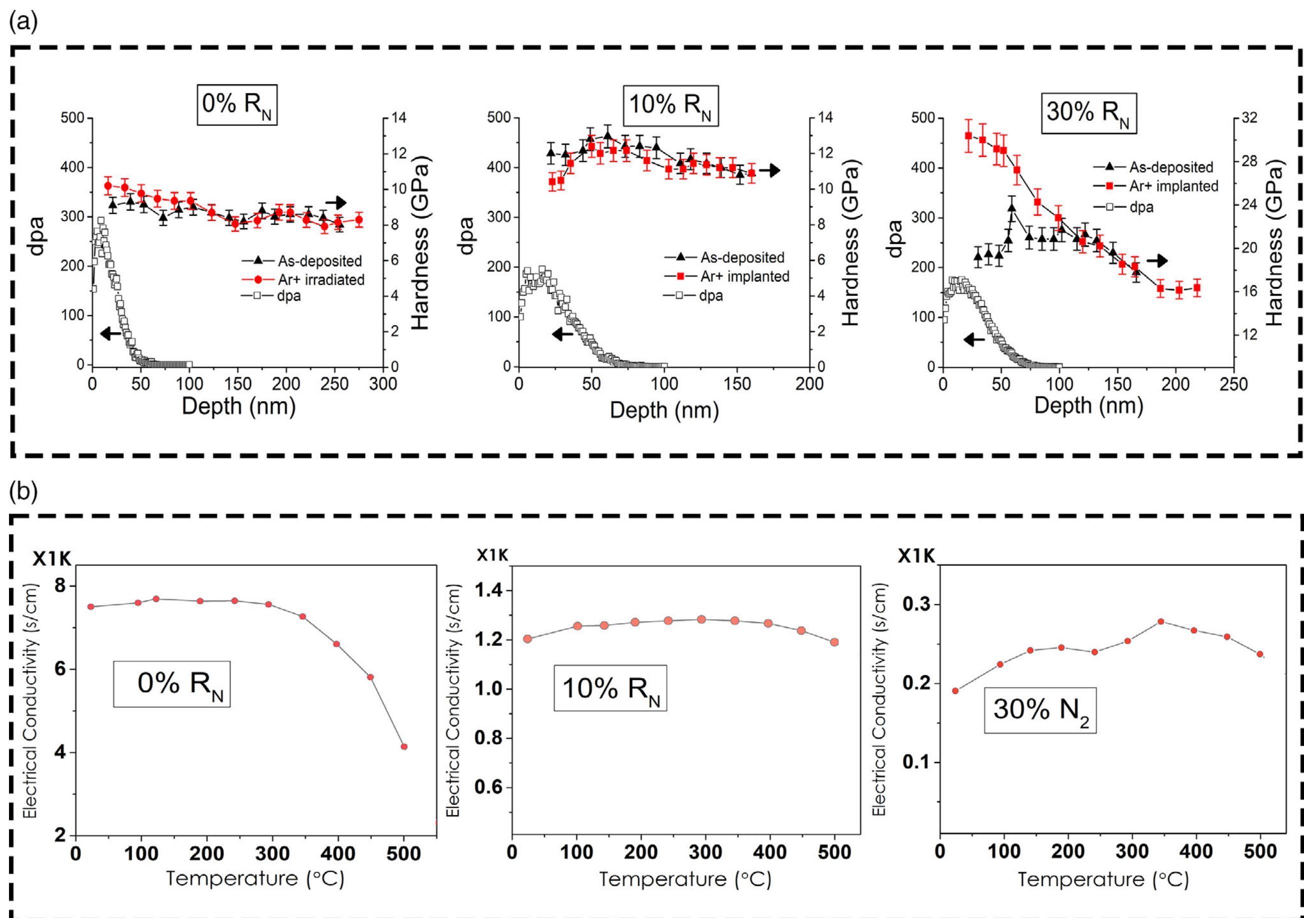

Figure 4. a) Displacements per atom (dpa) and Hardness versus indentation depth plot before and after Ar-ion irradiation; b) Electrical conductivity versus temperature plot of HfMoNbTaTiVWZr high-entropy film deposited at different R_N.

conductivity in high-entropy nitride films can be related to the presence of high lattice distortion in the films, which reduces the mean free path due to electron scattering.[53–55] Further investigation will be carried out to analyze the effect of Ar-ion irradiation and electrical conductivity on crystal structure, valence electron states, and microstructural changes of high-entropy TFMG and derived nitride films.

The fabrication of high-entropy films and nitrides using partially sintered targets is beneficial due to the lower cost and time required to develop new high throughput compositions. Furthermore, the composition, film thickness, and properties can be further controlled with different sputtering parameters. The use of a large number of principal elements with strong bonding and nitride forming ability can be beneficial to developing new high strength and extremely ductile TFMG and superhard nitride films for different applications. In the present research, HfMoNbTaTiVWZr high-entropy nitride films display enhanced hardness, compressive strength, and ductility, especially in 30% R_N high-entropy nitride film, which has to the best of our knowledge not yet been reported. Furthermore, the increase in lattice distortion arising from the larger number of principal elements is not only beneficial to mechanical properties, but also to the electrical properties and irradiation resistance of high-entropy alloys as well.

3. Conclusion

The current findings show the benefits of using high configurational entropy and strong nitride forming elements to enhance the strength and density of bonds resulting in high-entropy-based TFMG and its nitrides with superior mechanical properties. The high density of strong bonds in HfMoNbTaTiVWZr TFMG resulted in high ductility and thermal stability of up to ≈60% strain and 750 °C, respectively. Furthermore, the TFMG showed fewer changes in hardness values after Ar-ion irradiation due to the absence of phase transformation. Films deposited in the nitrogen atmosphere showed amorphous and nanocrystalline nitride films with increasing nitrogen content with high thermal stability up to 950 °C. The micro-compression of nitride film showed high hardness, yield strength, and ductility of up to 18.7 ± 2.5 GPa, 10.2 ± 0.4 GPa, and 30%, respectively, due to strong nitrides and lattice distortion. Furthermore, the high amount of lattice distortion in nitride film led to the very low

 © 2022 Wiley-VCH GmbH

electrical conductivity of 400 S cm^{-1} and behaved as an insulating material at higher temperatures. The Ar-ion irradiation on nitride film resulted in increasing the hardness by ≈3–11 GPa up to ≈80 nm depth. The extraordinary thermal stability, mechanical, electrical, and irradiation resistant properties of high-entropy-based TFMG and its nitrides offers a strong motivation to pursue high-entropy film compositions with higher configuration entropy and stronger bonding density.

4. Experimental Section

Film Deposition and Microstructure Characterization: A partially sintered target of HfMoNbTaTiVWZr was developed using 99.9% pure elemental powders mixed in plastic vials packed under Ar atmosphere, followed by partial sintering in SPS (Dr. Sinter 825, Fuji Electronic Industrial Co., Ltd., Japan) at 1200 °C in a vacuum with a heating rate of 100 °C min^{-1} and holding time of 5 min. The EDS mapping and elemental analysis on the cross-section of the target are shown in Figure S5 and Table S3, Supporting Information, respectively. HfMoNbTaTiVWZr high-entropy film was deposited on Si-substrate using DC-magnetron sputtering (Moorfield, London, UK) with sputtering power of 150 W and substrate rotation speed of 8 rpm without any substrate bias or substrate temperature. The target material was pre-sputtered for 5 min before the deposition to remove surface oxides and contaminants. The sputtering chamber was evacuated to a background pressure of 1.16×10^{-3} Pa. Ar gas with high purity was introduced into the chamber at a flow rate of 20 sccm. For developing HfMoNbTaTiVWZr high-entropy nitride films, N_2 flow ratio ($R_N = N_2/(N_2 + Ar)$) was adjusted at 10% and 30%, while other parameters were kept the same as for metallic films.

X-Ray diffraction (XRD) analysis was carried out using Cu-Kα radiation in PANalytical Empyrean (Empyrean, PANalytical, Malvern, UK) operating at 40 kV and 40 mA. Scans were performed between the 2θ range of 5° and 100° with 10 mm divergence slit and 1° diffracted beam slits. High-temperature thermal stability of the films was tested using in situ high-temperature XRD analysis equipped with an Anton Paar HTK 1200 N furnace (Empyrean, PANalytical, Malvern, UK). The furnace was heated with a heating rate of 10 °C min^{-1} up to 800 °C (0% R_N) and 1000 °C (10% R_N and 30% R_N), followed by 30 min stabilisation at every 50 °C interval and performing an XRD scan between the 2θ range of 15° and 50°. The lattice strain in 30% R_N film after in situ high-temperature XRD analysis was estimated with full-width half maximum of the peaks at 2θ angle of 35.3° and 40.8° using HighScore plus. The surface and cross-section morphology of the film was carried out using a Scanning Electron Microscopy Magellan 400 XHR-SEM equipped with EDS analysis (FEI Company, Eindhoven, Netherlands). The electron diffraction, microstructure, and STEM imaging were performed on an aberration-corrected transmission electron microscope (TEM) Themis Z (Thermo Fisher Scientific). A four-quadrant Super-X EDX detector was used to collect elemental maps.

Nano-Mechanical Characterization: Nano-hardness tests were conducted using in situ SEM with an Alemnis nano-indenter equipped with a diamond Berkovich tip with a maximum 10 mN load. It was freshly calibrated on a reference-fused silica sample. The effect of tip compression and any drift of equipment was corrected by software supplied by the manufacturer. Data gathered after the correction was analysed with the use of software supplied by the manufacturer of the device. Hardness and Young's Modulus were calculated with the Oliver and Pharr method using the same software. From the unloading part of the curve top (maximum) 5% and bottom (minimum) 30% were ignored for model fitting. Although it is not necessary for the Oliver and Pharr method to calculate hardness or Young's Modulus, it was done to check if any pile-up or sink-in was present.

Micropillars on each sample were etched with the use of a Focused Ion Beam (FIB). The general flow of the process was to mill rings in the material, each starting at the outer diameter and milling towards the centre. Milling was done in three steps: coarse (30 kV, 3 nA), slow (30 kV, 200 pA), and precise (30 kV, 2 pA). Schematics and examples of the result are presented in Figure S6, Supporting Information. As each sample was slightly different, each was etched with slightly different parameters (time, dose). The desired result was a pillar with height equal to layer thickness – in other words, to mill only the layer of material and to not mill substrate to have a well-defined boundary pillar-substrate. This helps to mitigate unwanted sink-in of a pillar. The target diameter of the pillar in each case was 800 nm. Five pillars were compressed for 0% R_N and ten pillars were compressed for 10% R_N and 30% R_N films. The number of pillars compressed in 0% R_N was lower than in other films due to negligible scattering in micro-compression. After fabrication, each pillar was imaged with SEM for measuring the pillar diameter and height. The actual height of the pillars was calculated taking into account the angle at which the SEM image was taken. Analysis of the data for each pillar was done with the exact parameters of the pillar and a summary of the measurements of diameter and height are shown in Table S4, Supporting Information.

Electrical Conductivity Measurement: High-entropy films with different R_N ratios were deposited for 60 min on an insulating sapphire wafer substrate (surface roughness (Ra): 8 ± 2 nm) with similar deposition conditions as mentioned above. The electrical measurements were carried out in a vacuum environment (≈5.3×10^{-2} mbar) in a two probe geometry using SBA458 Nemesis (Netzsch GmbH, Germany). Prior to measurements, the probe chamber was purged via nitrogen gas to avoid possible ambient interference on the films. The insulating sapphire substrate was selected to withstand high-temperature ramps without any contribution of the electrical properties to the films.

Ar-Ion Irradiation: Ion irradiation of Ar was performed to investigate the irradiation resistance of the created materials treated by a beam of high-energy ions. Irradiation was performed using a typical semi-industrial implanter IMJON (Institute of Fundamental Technological Research, PAS, Warsaw) with an energy of 45 keV and fluency of 1×10^{17} ions cm^{-2}. The evolution of the sample temperatures as a function of irradiation time was as follows: the temperature of the samples starts from room temperature, then monotonically increases and achieves values of 132 °C at the end of the irradiation process. Displacements per atom (dpa) as a function of depth was determined with the use of SRIM code according to the procedure described in the literature.[56] For 0% R_N, 10% R_N, and 30% R_N films, the maximal dpa was equal to 292, 196, and 175, respectively. Nano-indentation of irradiated films was measured using in situ SEM with an Alemnis nano-indenter equipped with a diamond Berkovich tip. Multi-cycle indentation was applied to obtain the depth profiles of the hardness changes and to compare them with the non-irradiated samples. Fifteen cycles from 1 to 15 mN were performed every 1 mN. The investigation of the unloading curves was performed with the same procedure as described above for as-deposited high-entropy films.

Materials Modeling: First principle modeling was performed for the high-entropy nitride film obtained at 30% R_N using density functional theory (DFT) as implemented in the Vienna Ab initio Simulation Package (VASP).[57–59] Using a plane wave basis set, the projector-augmented wave method[60,61] and the Perdew-Burke-Ernzerhof (GGA-PBE) exchange-correlation functional.[62] Non spin polarized calculations were performed (ISPIN = 1) using a plane wave energy cutoff of 600 eV and a gamma centered k-point grid with minimum spacing of 0.31 Å^{-1}. In all calculations the electronic self-consistent loop was converged to 10^{-6} eV using no symmetry constraints (ISYM = 0) and high precision (PREC = Accurate). To reduce the noise in forces an additional support grid for the evaluation of the augmentation charges was used (ADDGRID =.TRUE). The Methfessel-Paxton scheme[63] (ISMEAR = 1) for partial occupancies was used and the smearing width was set to 0.05 eV. For each element the following pseudopotentials where used: Ta_sv_GW, Zr_sv_GW, Hf_sv_GW, Mo_sv_GW, W_sv_GW, Nb_sv_GW, V_sv_GW, Ti_sv_GW and N_GW.

To account for the local substitutional disorder, the high-entropy nitride film was modeled using special quasirandom structures (SQS)[64,65] of size 128 atoms with an equiatomic composition, $(Ti_{1/8}Nb_{1/8}Mo_{1/8}Zr_{1/8}Hf_{1/8}W_{1/8}V_{1/8}Ta_{1/8})N$. The SQS were relaxed using the conjugate gradient method (IBRION = 2) until the maximum forces and stress were smaller than 10^{-2} eV Å^{-1} and 10^{-2} eV Å^{-3}, respectively. For the fully relaxed SQS the 6×6 elasticity tensor was calculated

© 2022 Wiley-VCH GmbH

following the method described by Jong et al.[66] Here the relaxed SQS are deformed using 6 unique deformation modes where each deformation is applied individually to the SQS. Atomic positions of the deformed SQS are then relaxed using VASP and the stress tensor is calculated. The elastic tensor was then obtained by a least-squares-fit of the applied strain and calculated stress tensors for all deformed structures. Here the Python Materials Genomics[67,68] (pymatgen) Python library was used to generate the deformed structures and to fit the elastic tensor using the applied strain and the calculated stress tensors. From the elasticity tensor, the mechanical properties of the high-entropy nitride film were calculated using the equations derived by Voigt and Reuss.[69]

Supporting Information

Supporting Information is available from the Wiley Online Library or from the author.

Acknowledgement

This work was supported by the Swedish Foundation for Strategic Research (SSF) for Infrastructure Fellowship grant no. RIF14-0083. And was enabled by the computational resources provided by the Swedish National Infrastructure for Computing (SNIC 2021/5-103) at HPC2N in Umeå and NSC in Linköping, partially funded by the Swedish Research Council through grant agreement no. 2018-05973. The present research was partially supported by the Polish National Science Centre, Grant 2015/19/D/ST8/03200.

Conflict of Interest

The authors declare no conflict of interest.

Data Availability Statement

The data that support the findings of this study are available from the corresponding author upon reasonable request.

Keywords

high-entropy alloy, high-entropy nitride film, high temperature, micro-compression, thin film metallic glasses

Received: January 5, 2022
Revised: March 29, 2022
Published online:

[1] A. Inoue, A. Takeuchi, *Acta Mater.* **2011**, *59*, 2243.
[2] C. J. Chen, J. C. Huang, H. S. Chou, Y. H. Lai, L. W. Chang, X. H. Du, J. P. Chu, T. G. Nieh, *J. Alloys Compd.* **2009**, *483*, 337.
[3] J. P. Chu, C. T. Liu, T. Mahalingam, S. F. Wang, M. J. O'keefe, B. Johnson, C. H. Kuo, *Phys. Rev. B: Condens. Matter Mater. Phys.* **2004**, *69*, 1.
[4] J. P. Chu, J. S. C. Jang, J. C. Huang, H. S. Chou, Y. Yang, J. C. Ye, Y. C. Wang, J. W. Lee, F. X. Liu, P. K. Liaw, Y. C. Chen, C. M. Lee, C. L. Li, C. Rullyani, *Thin Solid Films* **2012**, *520*, 5097.
[5] P. T. Chiang, G. J. Chen, S. R. Jian, Y. H. Shih, J. S. C. Jang, C. H. Lai, *Fooyin J. Health Sci.* **2010**, *2*, 12.
[6] F. X. Liu, P. K. Liaw, W. H. Jiang, C. L. Chiang, Y. F. Gao, Y. F. Guan, J. P. Chu, P. D. Rack, *Mater. Sci. Eng. A.* **2007**, *468–470*, 246.
[7] C. J. Lee, H. K. Lin, S. Y. Sun, J. C. Huang, *Appl. Surf. Sci.* **2010**, *257*, 239.
[8] N. Tüten, D. Canadinc, A. Motallebzadeh, B. Bal, *Intermetallics.* **2019**, *105*, 99.
[9] S. Hata, T. Kato, T. Fukushige, A. Shimokohbe, *Microelectron. Eng.* **2003**, *67–68*, 574.
[10] A. Takeuchi, N. Chen, T. Wada, Y. Yokoyama, H. Kato, A. Inoue, J. W. Yeh, *Intermetallics.* **2011**, *19*, 1546.
[11] Y. H. Liu, T. Fujita, A. Hirata, S. Li, H. W. Liu, W. Zhang, A. Inoue, M. W. Chen, *Intermetallics.* **2012**, *21*, 105.
[12] S. Zhao, H. Wang, L. Xiao, N. Guo, D. Zhao, K. Yao, N. Chen, *Phys. E* **2017**, *94*, 100.
[13] B. Song, Y. Li, K. Wang, Z. Cong, B. Gao, Z. Song, J. Chen, *Surf. Eng.* **2019**, *35*, 728.
[14] S. Fritze, C. M. Koller, L. von Fieandt, P. Malinovskis, K. Johansson, E. Lewin, P. H. Mayrhofer, *Materials* **2019**, *12*, 10.
[15] S. A. Alvi, H. Zhang, F. Akhtar, *Engineering Steels and High Entropy-Alloys* (Eds: A. Sharma, Z. Duriagina, S. Kumar), IntechOpen, London **2019**, https://doi.org/10.5772/intechopen.84991.
[16] P. K. Huang, J. W. Yeh, *J. Phys. D Appl. Phys.* **2009**, *42*, 115401.
[17] K.-H. Cheng, C.-H. Lai, S.-J. Lin, J.-W. Yeh, *Thin Solid Films.* **2011**, *519*, 3185.
[18] D. C. Tsai, Z. C. Chang, B. H. Kuo, T. N. Lin, M. H. Shiao, F. S. Shieu, *Surf. Coatings Technol.* **2014**, *240*, 160.
[19] D. C. Tsai, M. J. Deng, Z. C. Chang, B. H. Kuo, E. C. Chen, S. Y. Chang, F. S. Shieu, *J. Alloys Compd.* **2015**, *647*, 179.
[20] M. H. Tsai, C. H. Lai, J. W. Yeh, J. Y. Gan, *J. Phys. D Appl. Phys.* **2008**, *41*, 235402.
[21] Z. C. Chang, *Mater. Chem. Phys.* **2018**, *220*, 98.
[22] S. W. Kao, J. W. Yeh, T. S. Chin, *J. Phys. Condens. Matter.* **2008**, *20*, 145214.
[23] P.-K. Huang, J.-W. Yeh, *Surf. Coatings Technol.* **2009**, *203*, 1891.
[24] V. Braic, A. Vladescu, M. Balaceanu, C. R. Luculescu, M. Braic, *Surf. Coatings Technol.* **2012**, *211*, 117.
[25] J. H. Kang, K. J. Kim, *J. Appl. Phys.* **1999**, *86*, 346.
[26] S. C. Liang, Z. C. Chang, D. C. Tsai, Y. C. Lin, H. S. Sung, M. J. Deng, F. S. Shieu, *Appl. Surf. Sci.* **2011**, *257*, 7709.
[27] P. K. Huang, J. W. Yeh, *Scr. Mater.* **2010**, *62*, 105.
[28] Y.-W. Chung, W. D. Sproul, *MRS Bull.* **2003**, *28*, 164.
[29] H. W. Chang, P. K. Huang, J. W. Yeh, A. Davison, C. H. Tsau, C. C. Yang, *Surf. Coatings Technol.* **2008**, *202*, 3360.
[30] V. Hasannaeimi, S. Muskeri, B. Gwalani, D. C. Hofmann, S. Mukherjee, *Mater. Today Commun.* **2020**, *24*, 101237.
[31] C. A. Schuh, T. C. Hufnagel, U. Ramamurty, *Acta Mater.* **2007**, *55*, 4067.
[32] Y. Wang, J. Li, A. V. Hamza, T. W. Barbee, *Proc. Natl. Acad. Sci.* **2007**, *104*, 11155.
[33] G. Dehm, H. P. Wörgötter, S. Cazottes, J. M. Purswani, D. Gall, C. Mitterer, D. Kiener, *Thin Solid Films* **2009**, *518*, 1517.
[34] I. El Azhari, J. Garcia, M. Zamanzade, F. Soldera, C. Pauly, L. Llanes, F. Mücklich, *Acta Mater.* **2018**, *149*, 364.
[35] S. Kiani, C. Ratsch, A. M. Minor, S. Kodambaka, J. M. Yang, *Philos. Mag.* **2015**, *95*, 985.
[36] H. Fager, J. M. Andersson, J. Jensen, J. Lu, L. Hultman, *J. Vac. Sci. Technol. A* **2014**, *32*, 061508.
[37] S. H. Jhi, J. Ihm, S. G. Loule, M. L. Cohen, *Nature* **1999**, *399*, 132.
[38] W. A. Grant, *J. Vac. Sci. Technol.* **1978**, *15*, 1644.
[39] H. Jia, C. I. Muntele, L. Huang, X. Li, G. Li, T. Zhang, W. He, P. K. Liaw, *Intermetallics* **2013**, *41*, 35.
[40] J. Carter, E. G. Fu, G. Bassiri, B. M. Dvorak, N. David Theodore, G. Xie, D. A. Lucca, M. Martin, M. Hollander, X. Zhang, L. Shao, *Nucl. Instrum. Methods Phys. Res. Sect. B* **2009**, *267*, 1518.

© 2022 Wiley-VCH GmbH

[41] M. Iqbal, J. I. Akhter, Z. Q. Hu, H. F. Zhang, A. Qayyum, W. S. Sun, *J. Non. Cryst. Solids.* **2007**, *353*, 2452.
[42] L. Romano, G. Impellizzeri, L. Bosco, F. Ruffino, M. Miritello, M. G. Grimaldi, *J. Appl. Phys.* **2012**, *111*, 2.
[43] M. Popovic, M. Novakovic, Z. Rakocevic, N. Bibic, *Process. Appl. Ceram.* **2011**, *5*, 19.
[44] A. J. Perry, Y. P. Sharkeev, D. E. Geist, S. V. Fortuna, *J. Vac. Sci. Technol. A* **1999**, *17*, 1848.
[45] M. Popović, M. Novaković, N. Bibić, *Mater. Charact.* **2009**, *60*, 1463.
[46] M. Popović, M. Novaković, A. Traverse, K. Zhang, N. Bibić, H. Hofsäss, K. P. Lieb, *Thin Solid Films.* **2013**, *531*, 189.
[47] A. M. Vora, A. L. Gandhi, *Philos. Mag. Lett.* **2020**, *100*, 154.
[48] X. Feng, J. Zhang, Z. Xia, W. Fu, K. Wu, G. Liu, J. Sun, *Mater. Lett.* **2018**, *210*, 84.
[49] H. Zhang, Y. Z. He, Y. Pan, S. Guo, *J. Alloys Compd.* **2014**, *600*, 210.
[50] E. Österlund, G. Ross, M. A. Caro, M. Paulasto-Kröckel, A. Hollmann, M. Klaus, M. Meixner, C. Genzel, P. Koppinen, T. Pensala, A. Žukauskaitė, M. Trebala, *Phys. Rev. Mater.* **2021**, *5*, 035001.
[51] K. von Fieandt, L. Riekehr, B. Osinger, S. Fritze, E. Lewin, *Surf. Coatings Technol.* **2020**, *389*, 125614.
[52] H. Treichel, E. Eckstein, W. Kern, *Ceram. Int.* **1996**, *22*, 435.
[53] Y. Zhang, T. Zuo, Y. Cheng, P. K. Liaw, *Sci. Rep.* **2013**, *3*, 1.
[54] W. Huo, X. Liu, S. Tan, F. Fang, Z. Xie, J. Shang, J. Jiang, *Appl. Surf. Sci.* **2018**, *439*, 222.
[55] Y. Zheng, M. Zou, W. Zhang, D. Yi, J. Lan, C. W. Nan, Y. H. Lin, *J. Adv. Ceram.* **2021**, *10*, 377.
[56] R. E. Stoller, M. B. Toloczko, G. S. Was, A. G. Certain, S. Dwaraknath, F. A. Garner, *Nucl. Instrum. Methods Phys. Res. Sect. B* **2013**, *310*, 75.
[57] G. Kresse, J. Hafner, *Phys. Rev. B* **1993**, *47*, 558.
[58] G. Kresse, J. Furthmüller, *Comput. Mater. Sci.* **1996**, *6*, 15.
[59] G. Kresse, J. Furthmüller, *Phys. Rev. B* **1996**, *54*, 11169.
[60] P. E. Blöchl, *Phys. Rev. B* **1994**, *50*, 17953.
[61] G. Kresse, D. Joubert, *Phys. Rev. B* **1999**, *59*, 1758.
[62] J. P. Perdew, K. Burke, M. Ernzerhof, *Phys. Rev. Lett.* **1996**, *77*, 3865.
[63] M. Methfessel, A. T. Paxton, *Phys. Rev. B.* **1989**, *40*, 3616.
[64] A. Zunger, S.-H. Wei, L. G. Ferreira, J. E. Bernard, *Phys. Rev. Lett.* **1990**, *65*, 353.
[65] S.-H. Wei, L. G. Ferreira, J. E. Bernard, A. Zunger, *Phys. Rev. B.* **1990**, *42*, 9622.
[66] M. de Jong, W. Chen, T. Angsten, A. Jain, R. Notestine, A. Gamst, M. Sluiter, C. Krishna Ande, S. van der Zwaag, J. J. Plata, C. Toher, S. Curtarolo, G. Ceder, K. A. Persson, M. Asta, *Sci. Data* **2015**, *2*, 150009.
[67] S. P. Ong, W. D. Richards, A. Jain, G. Hautier, M. Kocher, S. Cholia, D. Gunter, V. L. Chevrier, K. A. Persson, G. Ceder, *Comput. Mater. Sci.* **2013**, *68*, 314.
[68] S. P. Ong, S. Cholia, A. Jain, M. Brafman, D. Gunter, G. Ceder, K. A. Persson, *Comput. Mater. Sci.* **2015**, *97*, 209.
[69] R. Hill, *Proc. Phys. Soc. Sect. A* **1952**, *65*, 349.

© 2022 Wiley-VCH GmbH